

Near-Intrinsic Energy Resolution for 30 to 662 keV Gamma Rays in a High Pressure Xenon Electroluminescent TPC

V. Álvarez^a, F.I.G.M. Borges^b, S. Cárcel^a, J. Castel^c, J.M. Catalá^d,
S. Cebrián^c, A. Cervera^a, C.A.N. Conde^b, T. Dafni^c, T.H.V.T. Dias^b,
J. Díaz^a, M. Egorov^e, R. Esteve^d, P. Evtoukhovitch^f, L.M.P. Fernandes^b,
P. Ferrario^a, A.L. Ferreira¹, E. Ferrer-Ribas^h, E.D.C. Freitas^b,
V.M. Gehman^e, A. Gil^a, I. Giomataris^h, A. Goldschmidt^{e,*}, H. Gómez^c,
J.J. Gómez-Cadenas^a, K. González^a, D. González-Díaz^c, R.M. Gutiérrezⁱ,
J. Hauptman^j, J.A. Hernando Morata^k, D.C. Herrera^c, V. Herrero^d,
F.J. Iguaz^c, I.G. Irastorza^c, V. Kalinnikov^f, L. Labarga¹, I. Liubarsky^a,
J.A.M. Lopes^b, D. Lorca^a, M. Losadaⁱ, G. Luzón^c, A. Mari^d,
J. Martín-Albo^a, A. Martínez^a, T. Miller^e, A. Moiseenko^f, F. Monrabal^a,
C.M.B. Monteiro^b, J.M. Monzó^d, F.J. Mora^d, L.M. Moutinho^g, J. Muñoz
Vidal^a, H. Natal da Luz^b, G. Navarroⁱ, M. Nebot^a, D. Nygren^e,
C.A.B. Oliveira^{e,g}, R. Palma^m, J. Pérezⁿ, J.L. Pérez Aparicio^m, J. Renner^e,
L. Ripoll^o, A. Rodríguez^c, J. Rodríguez^a, F.P. Santos^b, J.M.F. dos Santos^b,
L. Seguí^c, L. Serra^a, D. Shuman^e, A. Simón^a, C. Sofka^p, M. Sorel^a,
J.F. Toledo^d, A. Tomás^c, J. Torrent^o, Z. Tsamalaidze^f, D. Vázquez^k,
E. Velicheva^f, J.F.C.A. Veloso^g, J.A. Villar^c, R.C. Webb^p, T. Weber^e,
J. White^p, N. Yahlali^a

^a*Instituto de Física Corpuscular (IFIC), CSIC & Universitat de València, Calle
Catedrático José Beltrán, 2, 46980 Paterna, Valencia, Spain*

^b*Departamento de Física, Universidade de Coimbra, Rua Larga, 3004-516 Coimbra,
Portugal*

^c*Laboratorio de Física Nuclear y Astropartículas, Universidad de Zaragoza, Calle Pedro
Cerbuna 12, 50009 Zaragoza, Spain*

^d*Instituto de Instrumentación para Imagen Molecular (I3M), Universitat Politècnica de
València, Camino de Vera, s/n, Edificio 8B, 46022 Valencia, Spain*

^e*Lawrence Berkeley National Laboratory (LBNL), 1 Cyclotron Road, Berkeley,
California 94720, USA*

^f*Joint Institute for Nuclear Research (JINR), Joliot-Curie 6, 141980 Dubna, Russia*

^g*Institute of Nanostructures, Nanomodelling and Nanofabrication (i3N), Universidade de*

*Corresponding author

Email address: agoldschmidt@lbl.gov (A. Goldschmidt)

- Aveiro, Campus de Santiago, 3810-193 Aveiro, Portugal*
- ^h*IRFU, Centre d'Études Nucléaires de Saclay (CEA-Saclay), 91191 Gif-sur-Yvette, France*
- ⁱ*Centro de Investigaciones en Ciencias Básicas y Aplicadas, Universidad Antonio Nariño, Carretera 3 este No. 47A-15, Bogotá, Colombia*
- ^j*Department of Physics and Astronomy, Iowa State University, 12 Physics Hall, Ames, Iowa 50011-3160, USA*
- ^k*Instituto Gallego de Física de Altas Energías (IGFAE), Univ. de Santiago de Compostela, Campus sur, Rúa Xosé María Suárez Núñez, s/n, 15782 Santiago de Compostela, Spain*
- ^l*Departamento de Física Teórica, Universidad Autónoma de Madrid, Campus de Cantoblanco, 28049 Madrid, Spain*
- ^m*Dpto. de Mecánica de Medios Continuos y Teoría de Estructuras, Univ. Politècnica de València, Camino de Vera, s/n, 46071 Valencia, Spain*
- ⁿ*Instituto de Física Teórica (IFT), UAM/CSIC, Campus de Cantoblanco, 28049 Madrid, Spain*
- ^o*Escola Politècnica Superior, Universitat de Girona, Av. Montilivi, s/n, 17071 Girona, Spain*
- ^p*Department of Physics and Astronomy, Texas A&M University, College Station, Texas 77843-4242, USA*

Abstract

We present the design, data and results from the NEXT prototype for Double Beta and Dark Matter (NEXT-DBDM) detector, a high-pressure gaseous natural xenon electroluminescent time projection chamber (TPC) that was built at the Lawrence Berkeley National Laboratory. It is a prototype of the planned NEXT-100 ^{136}Xe neutrino-less double beta decay ($0\nu\beta\beta$) experiment with the main objectives of demonstrating the near-intrinsic energy resolution at energies up to 662 keV and of optimizing the NEXT-100 detector design and operating parameters. Energy resolutions of $\sim 1\%$ FWHM for 662 keV gamma rays were obtained at 10 and 15 atmospheres and $\sim 5\%$ FWHM for 30 keV xenon x-rays. These results demonstrate that 0.5% FWHM resolutions for the 2,448 keV hypothetical neutrino-less double beta decay peak are

realizable. This energy resolution is a factor 6 to 20 better than that of the current leading $0\nu\beta\beta$ experiments using xenon in the liquid phase and thus represents a significant advancement.

Keywords: Xenon, HPXe, Energy Resolution, High-Pressure, TPC, Electroluminescence, Double Beta Decay, Neutrinoless, ^{136}Xe , Fano

1. Introduction

Neutrino-less double beta decay ($0\nu\beta\beta$) is a postulated[1] rare process in which a nucleus changes by two units of charge while emitting two electrons (or positrons) but without the emission of neutrinos. Should this decay happen in nature the sum of the energies of the two electrons is expected to be monoenergetic at exactly the Q-value of the nuclear decay ($Q_{\beta\beta}$, equal to the mass difference between the parent and daughter nuclei). A precise energy measurement can therefore greatly aid in the identification of the $0\nu\beta\beta$ process in the presence of other more common processes that produce either continuous energy deposition spectra or peaks at well known and well separated energies. The occurrence of $0\nu\beta\beta$ would imply that neutrinos are their own anti-particle[?], or Majorana particles. Should neutrinos prove to be Majorana particles the observed prevalence of matter over anti-matter in our universe could be explained through the Leptogenesis mechanism[?].

The ^{136}Xe isotope is one of the candidate nuclei in which $0\nu\beta\beta$, in this case $^{136}\text{Xe} \rightarrow ^{136}\text{Ba} + e^- + e^-$, could be detectable because the single beta decay which would otherwise dominate the experimental count rate is energetically forbidden. Two currently running experiments are searching for this rare process in ^{136}Xe . EXO [?] uses 200 kg of the enriched isotope in a cryogenic

20 liquid xenon Time Projection Chamber[?]] (TPC) and KamLAND-Zen [?
21] uses 330 kg of the isotope dissolved in 1,000 tons of organic scintillator.
22 The energy resolutions for these two experiments are 3-4% and 10% FWHM
23 respectively at the 2.458 MeV[?] $Q_{\beta\beta}$ of the ^{136}Xe decay. It is well known,
24 on the other hand, that xenon in gaseous phase can offer significantly better
25 energy resolution[2] due to its small Fano factor[?] $F=0.14$ (a measure of
26 the level of fluctuations in the number of ionization electrons). For a xenon
27 gas pressure of less than 40 atm the intrinsic energy resolution is expected to
28 be about 0.3% FWHM near the $Q_{\beta\beta}$. It is thus clear that a xenon detector
29 at moderately high pressure would represent a significant advantage for the
30 search of the $0\nu\beta\beta$ spectrum peak as long as its implementation can preserve
31 a near-intrinsic energy resolution.

32 NEXT-100 is an experiment[?] that is being constructed to search
33 for $0\nu\beta\beta$ using 100-150 kg of ^{136}Xe in a 10-15 atm TPC at the Canfranc
34 underground laboratory (LSC) under the Pyrenees mountains in Spain. In
35 the TPC, electrons liberated through ionization by the passage of energetic
36 charged particles (such as the two electrons from the $0\nu\beta\beta$ decay) will drift
37 under the presence of a weak electric field towards a small region with a
38 high electric field. The E/P (electric field divided by pressure) in this high
39 field region is such that electrons can gather enough energy to excite xenon
40 atoms, but not enough to ionize them. Most of the excitation energy is
41 ultimately released in the form of ultra-violet (UV) photons of wavelengths
42 near 170 nm and constitutes the electroluminescence (EL)[?] signal. For
43 each ionization electron thousands of EL photons can be produced. An array
44 of photomultiplier tubes (PMTs) then detects a fraction of the UV photons to

45 render a measurement of the total energy released in the gas with a statistical
46 precision near the Fano limit.

47 The NEXT-100 TPC will provide, in addition to a very precise energy
48 measurement, a 3-D image of the ionization tracks by means of a dense array
49 of silicon photomultipliers[?] (SiPMs or MPPCs) installed near the elec-
50 troluminescence region. This topological information is useful to distinguish
51 between events with 2 electrons emerging from a single point, such as in
52 $0\nu\beta\beta$, from the electrons that result from interactions of gamma rays from
53 natural radioactivity in detector and surrounding materials.

54 In this paper we present the design, data and results from the NEXT-
55 DBDM (NEXT prototype for Double Beta and Dark Matter) detector, a
56 1 kg natural xenon electroluminescent TPC that was built at the Lawrence
57 Berkeley National Laboratory. It is a prototype of the NEXT-100 detector
58 with the main objectives of demonstrating the near intrinsic energy resolution
59 at energies up to 662 keV and of optimizing the NEXT-100 detector design,
60 construction, and operating parameters.

61 **2. High Pressure Xenon Electroluminescent TPC**

62 The basic building blocks of the NEXT-DBDM xenon electroluminescent
63 TPC are: a stainless steel pressure vessel, a gas system that recirculates
64 and purifies the xenon at 10-15 atm, hexagonal meshes that establish high-
65 voltage equipotential planes in the boundaries of the drift and the EL region,
66 field cages with hexagonal cross sections to establish uniform electric fields
67 in those regions, an hexagonal pattern array of UV sensitive PMTs inside
68 the pressure vessel and an associated readout electronics and data acquisition

69 (DAQ) system.

70 When ionizing radiation traverses the drift region of the TPC, xenon
71 atoms are ionized or excited. Most of the excitation energy is promptly
72 released as a fast scintillation pulse of 172 nm UV photons that lasts 10-30
73 ns[?]. A fraction of these photons are detected in the PMT array, forming
74 the S1 signal that provides the start time t_0 for the TPC. The ionization (or
75 secondary) electrons, on the other hand, drift for a maximum distance of 8 cm
76 at a velocity of $0.1\text{cm}/\mu\text{s}$ towards the EL region. There they accelerate and
77 produce copious EL UV photons. The same PMT array detects a fraction of
78 these, forming the S2 signal.

79 In the NEXT-DBDM detector the PMT array and the EL region, which
80 are both hexagonal areas with 12.4 cm between opposite sides, are 13.5 cm
81 away from each other (see Fig.1). Thus point-like isotropic light produced
82 in the EL region illuminates relatively uniformly the PMT array. This geo-
83 metric configuration also makes the illumination pattern and the total light
84 collection only very mildly dependent on the position of the light origin within
85 the EL region. The diffuse reflectivity of the TPC walls increases this light
86 collection uniformity further. As a result, the device provides good energy
87 measurements with little dependence on the position of the charge deposi-
88 tions. On the other hand, without a light sensor array near the EL region as
89 in the current NEXT-DBDM, precise tracking information is not available
90 and only coarse average position can be obtained using the PMT array light
91 pattern.

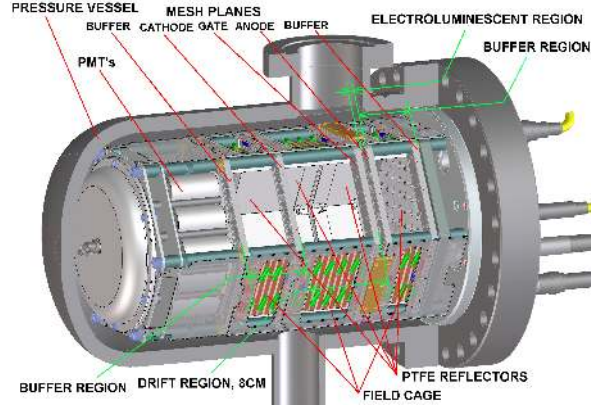


Figure 1: **NEXT-DBDM electroluminescent TPC configuration:** An array of 19 photomultipliers (PMTs) measures S1 primary scintillation light from the 8 cm long drift region and S2 light produced in the 0.5 cm electroluminescence (EL) region 13.5 cm away from the PMTs. Two 5 cm long buffer regions behind the EL anode mesh and between the PMTs and the cathode mesh grade the high voltages (up to ± 17 kV) down to ground potential.

92 3. Intrinsic Energy Resolution in the HPXe TPC

93 The intrinsic energy resolution in a xenon gas detector that measures
 94 ionization is given by:

$$\delta E/E = 2.35\sqrt{(FW_i/E)}FWHM \quad (1)$$

95 where E is the energy released in the detector, W_i is the average energy
 96 required to liberate an electron and F is the Fano factor that quantifies the
 97 fluctuations in the number of liberated electrons. While F and W_i are energy,
 98 drift field and pressure dependent due to electron-ion recombination and due
 99 to the energy dependence of the energy loss rate, dE/dx , their values are
 100 slowly varying in the range of energies, 30-662 keV, pressures, 10-17 atm,
 101 and drift fields, 0.3-2.0 kV/cm, studied here. For the purpose of studying

102 the energy resolution in the NEXT-DBDM detector we used 662 keV gamma
 103 rays from a ^{137}Cs source and 28-34 keV xenon x-rays that follow photoelectric
 104 interactions of the gamma rays. Thus, for $F=0.14$ [?] and $W_i=21.9$ eV[?
 105] the intrinsic energy resolutions are approximately 0.51% FWHM for 662
 106 keV and 2.3% FWHM for 30 keV.

107 **4. Experimental Aspects of the Energy Resolution in the Electro-** 108 **luminescent HPXe TPC**

109 *4.1. Statistical*

110 In the NEXT-DBDM detector the number of liberated electrons is not
 111 measured directly. Rather, those electrons are drifted and then accelerated
 112 to produce O(1000) UV photons each of which O(10) are measured as photo-
 113 electrons in the PMT array. This gain and measurement sequence introduces
 114 fluctuations beyond the intrinsic Fano limit. In Ref.[?] a formalism was
 115 developed to calculate the energy resolution achievable in light of those ad-
 116 ditional fluctuations:

$$\delta E/E = 2.35\sqrt{((F + G)W_i/E)\text{FWHM}} \quad (2)$$

117 with

$$G = 1/\eta + (1 + \sigma_{pd}^2)/n_{pe} \quad (3)$$

118 where η is the average number of UV photons produced in the EL region per
 119 secondary electron (or optical gain), n_{pe} is the average number of photons
 120 detected (as photoelectrons) per secondary electron and σ_{pd}^2 is the variance on
 121 the charge measured for single photoelectrons. In the absence of afterpulsing
 122 or noise the charge variance for a typical PMT is $\sigma_{pd}^2 = 0.5$ or less.

123 The electroluminescence optical gain in pure high pressure xenon is given
124 approximately by[?]:

$$\eta = 140 \left(\frac{\Delta V}{p \Delta z} - 0.83 \right) \cdot p \cdot \Delta z \quad (4)$$

125 where ΔV is the voltage difference between the electrodes that form the EL
126 region in kilovolts, p is the pressure in atmospheres and Δz is the distance
127 between the electrodes in centimeters. For instance, if $p=10$ atm, $\Delta V=11.3$
128 kV and $\Delta z=0.5$ cm the EL optical gain is $\eta=1000$.

129 The value of n_{pe} is the product of the EL optical gain η times the collec-
130 tion efficiency (the probability of a UV photon generated in the EL region
131 reaching a PMT window) times the PMT quantum efficiency at the corre-
132 sponding wavelength. For example for a 10% collection efficiency, a 15%
133 PMT quantum efficiency at the 170 nm of the xenon electroluminescence
134 and $\eta=1000$, $n_{pe}=15$ and the expected energy resolution for 662 keV gamma
135 rays in the absence of systematic effects is 0.66% and 3.11% for 30 keV.

136 4.2. Systematic

137 Systematic effects that broaden the energy resolution can be grouped in
138 two categories: position and time dependencies. Position dependencies of the
139 energy response arise, for example, from a non-uniform EL light collection ef-
140 ficiency, a non-uniform EL gain, secondary electron losses due to attachment
141 on electronegative impurities during drift and secondary electrons hitting the
142 TPC walls due to diffusion or due to drift field non-uniformities. Time depen-
143 dencies of the energy response arise, for example, from time-varying voltages,
144 temperature (and its subsequent effect of gas viscosity, PMT response, etc),
145 gas flow and purity, PMT response and gas density.

146 In the NEXT-DBDM TPC systematic dependencies of the energy re-
147 sponse as a function of the position along the drift (z -axis in our chosen
148 coordinate system) are small due to the high xenon gas purity achieved. In
149 addition, the z position of charge depositions within the drift region is very
150 precisely measured. The opposite is true in the plane perpendicular to the
151 drift direction ($x - y$): the light collection changes more rapidly as a func-
152 tion of distance from the center axis of the TPC and the $x - y$ position of
153 charge depositions is poorly measured. For this reason, to study the energy
154 resolution achievable with the xenon EL TPC, calibration gamma rays are in-
155 troduced along the center z axis through a narrow aperture collimator. Still,
156 the actual charge depositions happen over an extended region in $x - y$ (and
157 z) due to the length of the electron tracks and due to the multi-site depo-
158 sitions from Compton scatters and from xenon x-rays following photoelectric
159 absorption.

160 **5. Experimental Setup**

161 *5.1. Gas System*

162 The main functions of the gas system are to recirculate and purify the
163 xenon at pressures up to 17 atm. A magnetically driven seal-less and oil-less
164 pressure rated (95 atm) pump manufactured by Pumpworks Inc. (model
165 2070) recirculates the xenon at room temperature at 5-15 standard liter per
166 minute (slpm). For the total system volume of approximately 10 liter at
167 10 atm pressure the pump recirculates one full volume in about 10 min-
168 utes. A pressure rated (18 atm) heated getter from Johnson Matthey (model
169 PureGuard) removes O_2 , H_2O , N_2 and many other impurities using a non-

170 evaporable zirconium-based material. The getter operates at a constant 450
 171 degrees Celsius irreversibly removing the impurities through bulk diffusion.

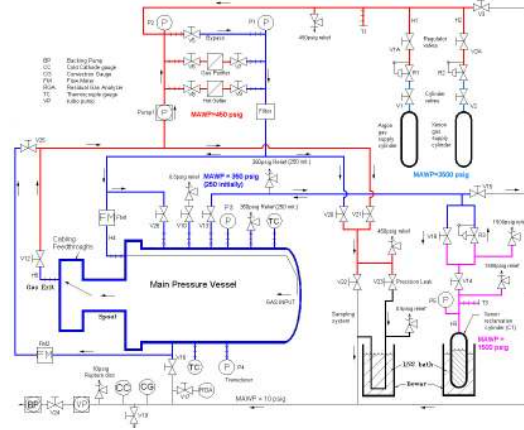



Figure 2: Gas system schematic (simplified).

172 In Figure 2 the complete gas system is shown. Besides the recircu-
 173 lation pump and the heated getter the system includes a vacuum system
 174 with a roughing pump (make  LiboVacDry), a turbomolecular pump (make
 175 Leybold-Heareus) and Pirani and ion vacuum gauges, a reclamation cylin-
 176 der where xenon is stored when it is cryogenically removed from the main
 177 pressure vessel, an argon purge system, a gas sampling system with a pre-
 178 cision leak valve and a residual gas analyzer (model SRS100) and a room
 179 temperature secondary getter (SAES model MicroTorr MCP190).

180 A set of pressure relief valves (with different settings for the various parts
 181 of the pressure rated system) and a burst disk in the vacuum system protect
 182 the equipment and personel from overpressure hazards.

183 The typical gas cycle during normal operation of the TPC consists of a
 184 vacuum step to 10^{-5} torr, followed by an argon purge and recirculation at 1

185 atm, a second vacuum step to remove the argon and then the xenon fill from
186 the reclamation cylinder. After the fill, the recirculation and purification
187 is started and monitored and controlled with gas flow meters (models Sierra
188 Smart-Trak and Omega FM1700) and a variac that powers the recirculation
189 pump to set the recirculation flow.

190 *5.2. Pressure Vessel and Feedthrough Ports*


191 The main pressure vessel is an 8.7 liter stainless steel cylindrical shell
192 of 20 cm diameter and 33.5 cm length with an elliptical head on one end and
193 a custom gasketed Conflat flange (main flange) on the other. Half inch VCR
194 ports on the side of the vessel are used for gas fill, recirculation flow, pressure
195 and temperature gauges and pressure relief valves. A 5.9 cm diameter (ID)
196 port is used for vacuum pumping. On the main flange there are small ports
197 with commercial high voltage feedthroughs (rated to 20 kV and 17 atm) with
198 additional custom PTFE sleeves on the inside to increase the breakdown
199 voltage when operating with high pressure xenon. A larger central port is
200 used to connect to an octagon-shaped vessel through a long tube with an
201 internal source reentrance tube with a 2mm thick endcap. Signal and high-
202 voltage coaxial cables from the (in-vessel) PMT array pass through the axial
203 extension tube and connect with 32-pin feedthroughs on the side ports of the
204 octagonal vessel.

205 *5.3. TPC*

206 The field configuration in the TPC is established by five stainless steel
207 meshes with 88% open area at 5 cm (cathode buffer or PMT mesh), 5.5
208 cm (cathode or drift start mesh), 13.5 cm (gate or EL-start mesh), 14.0 cm

221 the potential and produce a uniform electric field. The ceramic support
222 panels are connected, mechanically and electrically, to the outer perimeter
223 of the mesh support frames and to the first and last copper stripes on their
224 corresponding PTFE panel. High voltage connections to establish the TPC
225 fields (HHV) are made directly to the mesh frames.

226 Six short PEEK rods going through holes on the mesh frames' vertices
227 secure the anode and anode buffer meshes to the main vessel flange. Three
228 PEEK c-clamps (on alternate sides of the hexagon) with grooves to prevent
229 HV surface breakdown attach, in turn, the anode mesh to the gate mesh
230 maintaining a gas gap of 0.5 cm. Finally, six PEEK rods support the gate,
231 cathode and cathode buffer meshes as well as the 19-PMT array. Mechanical
232 tolerances obtained are better than 1 mm throughout the TPC geometry.

233 In the initial implementation of the NEXT-DBDM TPC longer PEEK
234 rods supported the entire assembly going through holes in the anode and
235 gate mesh frames with PEEK spacers to maintain the EL gap. High voltage
236 breakdown in the form of sparks across the gap during HV conditioning and
237 at random times thereafter produced conductive paths on the insulator sur-
238 face, requiring time consuming repair. The c-clamp solutioescribed above
239 made the TPC completely resilient to the unavoidable occasional sparking.

240 Clean gas from the purification system flows through an internal tube to
241 an enclosed volume behind the PMTs and reaches the active volume through
242 small dedicated PEEK tubes between the PMTs to exit the TPC through a
243 port on the octagonal vessel at the end of the extension tube.

244 A wide range of HHV voltages were used to investigate the TPC perfor-
245 mance dependence on drift electric field and on the E/P in the EL region:

246 cathode voltages from -4 to -13 kV, gate voltages from -1 to -10 kV and
247 anode voltages from 1 to 13 kV.

248 *5.4. PMTs, Readout and Data Processing*

249 The PMT array is composed of nineteen 2.54 cm diameter Hamamatsu
250 7378A PMTs. These PMTs, with fused silica windows, have a quantum
251 efficiency of $\sim 15\%$ for 170 nm xenon light. The PMTs were individually
252 pressure tested to 19 atm (absolute) and no mechanical or performance fail-
253 ures were observed. The HV, typically about -1000V, is individually set to
254 get a $\sim 10^6$ gain. The bases for the PMT array are implemented in a single
255 hexagonal PCB board with surface mount components and with pin sockets
256 that provide both mechanical support for the PMTs as well as the necessary
257 electrical connections. The base has about $1\text{ M}\Omega$, thus power dissipation is
258 about 1 Watt per PMT, and $1\ \mu\text{F}$ capacitors connected to the last dynode
259 stages to keep the gain constant during long EL light pulses. 200 pF capaci-
260 tors connected from the PMT anodes to ground slow down the return to the
261 baseline after a pulse so that all photoelectrons are properly sampled in the
262 100 MHz digitizers.

263 PMT anode signals travel through $\sim 1\text{ m}$ long PTFE coaxial cables to the
264 32-pin feedthroughs and then to 8-channel Phillips-777 amplifiers set to a gain
265 of 40. The amplified signals are then stretched and attenuated in a passive
266 RCR circuit to reduce high frequency noise and to match the input range of
267 the SIS3302 16-bit digitizers that sample the individual PMT signals at 100
268 mega-samples per second. PMT waveform data, typically 16,384 samples or
269 $163.84\ \mu\text{s}$, are readout through an SIS3150 USB to VME interface to a Linux
270 server for processing, analysis and storage. The overall system noise is such

271 that individual photoelectrons can be detected and the instantaneous (10 ns)
272 dynamic range per PMT is 1-to-200 photoelectrons. Custom-written DAQ
273 software is used to control the data acquisition.

274 The trigger is designed to identify S2 EL pulses. It is formed based
275 on a single PMT by a $12\mu\text{s}$ peaking-time shaping amplifier followed by a
276 discriminator. The trigger is used as a stop signal (with a stop delay) for the
277 digitizers such that there are, typically, $80\mu\text{s}$ of waveform data preceeding
278 the first S2 pulse and $80\mu\text{s}$ after. Since the maximum drift time is about
279 $80\mu\text{s}$, this permits the search for the S1 pulse in the offline analysis while
280 ensuring that all the S2 light from one event is measured.

281 After a block of 512 events is collected with about 100 MBytes in raw DAQ
282 data format, an automated process unpacks the data, applies calibration
283 constants to the individual PMTs and executes the analysis code based on
284 ROOT[?]] and FMWK[?]] that finds S1 and S2 pulses and computes
285 energies, times and positions and outputs the results in a 1 MBytes ROOT
286 data trees.

287 *5.5. Controls and Monitoring*

288 All system controls (except the single PMT HV power supply), such as
289 HHV voltage settings and current limits and recirculation flow, are done
290 manually. The three HHV voltages and currents, the PMT HV power supply
291 voltage, the pressure inside the TPC vessel, the temperature in two points in-
292 side the TPC and the room temperature are automatically and continuously
293 logged for monitoring and to aid in offline data analysis. The recirculation
294 flow is manually logged.

295 6. Data Analysis

296 In the first step of the data analysis the individual PMT waveforms are
297 changed to photoelectron units using calibration constants from dedicated
298 low occupancy single photoelectron runs with short LED light pulses. A
299 sum waveform is then computed from a sample-by-sample addition of the
300 19 PMTs' waveforms and the baseline of the sum waveform is obtained. A
301 search for S1 and S2 pulses that cross a threshold, determined from the
302 value of the baseline noise, follows. Pulses are defined as S1 candidates if
303 they are less than 500 ns wide, all other pulses are considered S2 candidates.
304 Individual pulses are integrated and the largest S1 candidate is assumed to
305 be the event's start time and the others discarded. All S2 pulses that follow
306 the chosen S1 are considered part of the event while the ones preceding it
307 are discarded. An event is considered valid if it has and S1 pulse with at
308 least one associated S2 pulse. Figures 4 and 5 show typical valid events from
309 662 keV ^{137}Cs gamma ray interactions.

310 During the automatic analysis of the data, the electron attachment life-
311 time of the gas is not yet known. In order to enable the offline correction
312 of these charge losses the ten first moments of the S2 charge distribution
313 $\int q(t)t^n dt$ with $n=0,1,\dots,9$ are calculated where t is the time interval since the
314 S1 start time pulse.

315 An average x-y position for the event is calculated from an S2-charge
316 weighted average of the PMT positions. The event is also time split into
317 equal-charge slices. For each slice an average x-y position is computed from
318 the PMT light distribution. This provides x-y-z positions for well separated
319 energy depositions such as from Compton scatters or from x-rays following

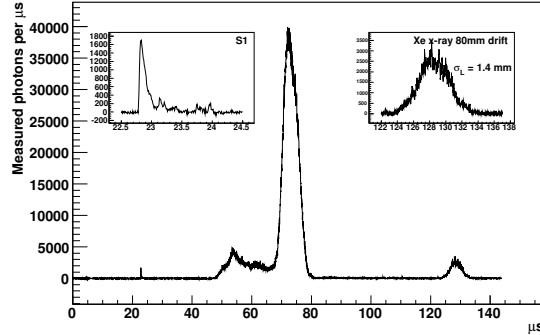


Figure 4: **Typical full energy 662 keV gamma ray event waveform:** the sum of the previously calibrated 19 photomultipliers' waveforms is shown. The S1 pulse (shown in detail in the left inset) due to xenon scintillation is short and with $O(200)$ measured photons. Two S2 pulses caused by electroluminescence of xenon from ionization electrons follow. The first with $\sim 270,000$ measured photons is likely due to a 630 keV electron from the photoelectric interaction of the 662 keV gamma ray; the pulse structure reflects the ionization density of the track along its ~ 2.5 cm long projection on the drift (z) direction. The second (shown in detail in the right inset) with $\sim 12,000$ measured photons is likely due to the interaction, a few cm away, of a 30 keV xenon x-ray following the photoelectric process; since the 30 keV energy deposition is nearly point-like the pulse shape is gaussian with a σ_L of 1.4 mm set by the longitudinal diffusion of the electrons during the ~ 8 cm drift. This event is from a data run taken at 10 atm with a 0.16 kV/cm drift electric field and an E/P of 2.1kV/(cm atm) in the EL region.

320 photoelectric interactions.

321 7. Results

322 7.1. PMT Performance

323 As shown in formulas 2 and 3 the energy resolution achievable in an elec-
 324 troluminescent TPC depends on the precision with which individual photons

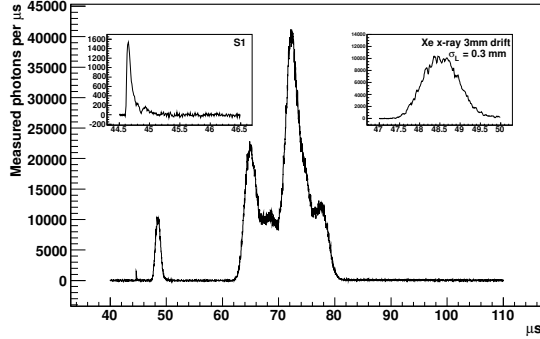


Figure 5: **A second typical full energy event:** In this event from the same data run as in Fig.4 the xenon x-ray interacted close to the EL region and thus the ionization electrons drifted for just 3mm and underwent a correspondingly small longitudinal diffusion σ_L of 0.3 mm.

325 can be measured. System noise and the variance from the avalanche mul-
 326 tiplication in the PMT (mostly from the first dynode stages) contribute to
 327 the spread of the charge measured for photoelectrons. It was found, how-
 328 ever, that the charge fluctuations due to PMT after-pulsing are the dominant
 329 factor in the photoelectron charge resolution. After-pulsing caused by the oc-
 330 casional ionization of residual gas molecules in the PMT vacuum volume can
 331 produce delayed pulses with large charges (10-20 photoelectron charges are
 332 not uncommon). Dedicated LED data runs with light pulses less than 100
 333 nsec long (first afterpulse peaks from hydrogen and helium ions appear at 200
 334 and 300 nsec for these small PMTs) were thus taken to assess the charge-
 335 variance for each PMT. The typical value was found to be $\sigma(Q)/Q = 1.2$
 336 thus $\sigma_{pd}^2=1.44$ with small PMT-to-PMT variations.

337 *7.2. Position Measurement*

338 The TPC configuration with the PMT array 13.5 cm from the EL re-
339 gion does not permit detailed track reconstruction in the x-y plane. Still,
340 the position reconstruction achievable allows the fiducialization of pulses to
341 select events/pulses within regions of the TPC with uniform light collection
342 efficiencies. The position reconstruction for isolated 50-100 keV energy de-
343 positions shown in Fig. 6 displays the hexagonal boundary of the TPC. A
344 scaling factor of ~ 30 is needed to convert charge-weighted average x and y
345 positions to true TPC xy coordinates.

346 Several data runs were taken with LED light pulses of various intensities
347 to determine the position resolution for point depositions of charge as a
348 function of the amount of light produced and detected. Figure 7 shows the
349 obtained position resolutions which approximately follow the expected $1/\sqrt{N}$
350 dependency on the photon statistics.

351 *7.3. Energy Measurement*

352 The energy measurement is derived from the summed waveform (in pho-
353 tons detected) of all S2 pulses following the event S1 pulse. Figure 8 shows
354 a calibrated spectrum obtained from the ^{137}Cs source collimated with the
355 gamma rays entering the chamber along its central axis. The full energy
356 peak events in this data run have $\sim 270,000$ detected photons which, for
357 $W_i=21.9$ eV, corresponds to about 8.9 photons detected per ionization (sec-
358 ondary) electron. Using the nominal EL gain $\eta=846$ from Eq.4 the total
359 number of photons produced is $846 \cdot 662,000/21.9 \simeq 25.5$ million. From this,
360 an S2-photon detection efficiency slightly larger than 1% is deduced.

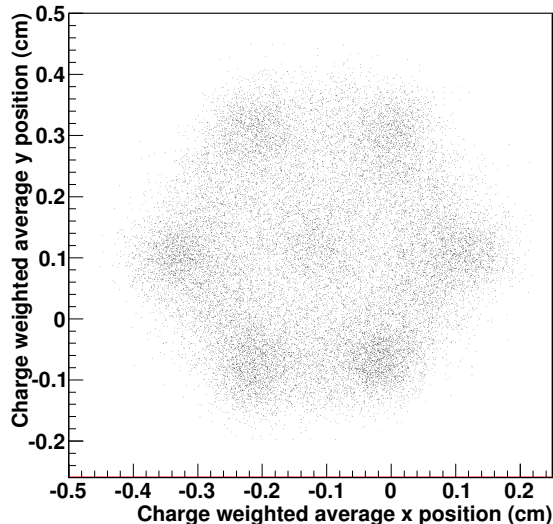


Figure 6: **Position reconstruction:** The charge-weighted average of the 19 PMT positions is used for x-y reconstruction. Events with energy depositions between 50 and 100 keV were selected; at these energies ionization tracks extend for just a few mm and produce enough light to reconstruct with sufficient position resolution. The edges of the hexagonal area correspond to the TPC cross section. Due to the spatial uniformity of the PMT plane illumination a scaling of factor of ~ 30 (not applied here) is needed to obtain true x-y positions from these charge-weighted averages. These data were taken with the ^{137}Cs source, at 10 atm and with E/P of $2\text{kV}/(\text{cm atm})$ in the EL region.

361 While the spectrum was calibrated only using the 662 keV line, the xenon
 362 x-rays peak appears at the correct energy (around 30 keV) confirming the
 363 expected linearity of the energy measurement in the interval of interest here.

364 Attachment losses of drifting secondary electrons can be assessed from the
 365 full energy peak position as a function of the drift time of the events. Figure
 366 9 shows typical data for 10 and 15 atm with excellent electron lifetimes of
 367 36 and 9 milliseconds, respectively. Less than 1% of the electrons are lost

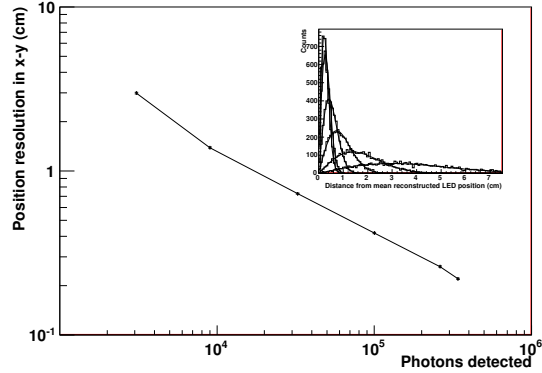


Figure 7: **Position resolution for LED light pulses:** The position resolution in the x-y plane as a function of the number of detected photons is shown. The resolution is derived from data from light pulses from an 378 nm LED located behind the PTFE backplane, which diffuses its light, and illuminates the PMT plane from about 19 cm distance. The inset shows the radial distributions (and fits) from which the individual resolution values were obtained.

368 to attachment for the maximum 8 cm drift length. Assuming that the main
 369 source of electron attachment is due to residual O₂, the measured electron
 370 lifetime at 10 atm corresponds to a residual oxygen component at the 2-4 part
 371 per billion. The lower lifetime at 15 atm is due to the pressure dependence
 372 of the 3-body attachment process rate.

373 The S2 photon collection efficiency is expected to vary somewhat as a
 374 function of the x-y position because of solid angle and chamber optics (wall
 375 reflectivities,etc). A sample of xenon x-ray energy depositions was used to
 376 measure the change in photon detection efficiency as a function of the radial
 377 position. Figure 10 shows this dependence derived from a run in which
 378 individual x-rays where reconstructed with ~ 0.8 cm resolution in x-y. For
 379 the purpose of this measurement x-ray depositions can be considered point-

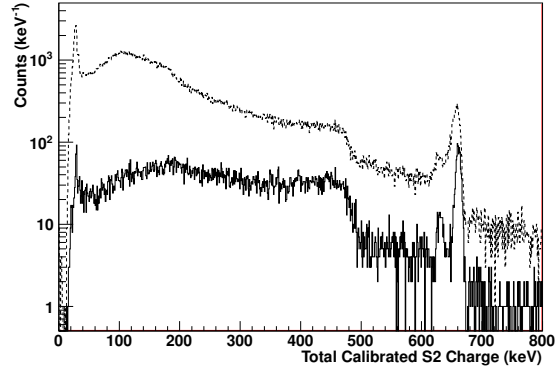


Figure 8: **Energy spectrum for ^{137}Cs 662 keV gamma rays:** The dashed line shows the calibrated spectrum (using the full energy 662 keV peak alone) from a data run taken at 10 atm with a 0.3 kV/cm drift electric field and an E/P of 2 kV/(cm atm) in the EL region. The 1 mCi source is heavily collimated and its gamma rays enter the TPC along the drift axis (z). Below the full energy peak at 662 keV, the smaller x-ray escape peak at ~ 630 keV, the Compton edge at 477 keV and the xenon x-ray peak at ~ 30 keV can be seen. The solid line is the same spectrum with a requirement that the reconstructed average position of an event be less than ~ 1.2 cm from the TPC axis. The small feature near 184 keV is due to Compton backscatters. The no-source background spectrum (not shown) has a broad peak near 100 keV.

380 like because 30 keV electron tracks at these pressures extend typically for less
 381 than half a millimeter. A nearly flat response is seen up to 2 cm radius and
 382 then a linear decline in response towards the outer edge of the TPC where
 383 the collection is about 10% lower than in the center.

384 In the absence of detailed track imaging, the radial dependence of the
 385 detector response to point-like depositions affects the TPC energy resolution
 386 for extended tracks. Electron tracks from 662 keV gamma interactions at
 387 the pressures of interest here have 2-4 cm spans and nearly random shapes

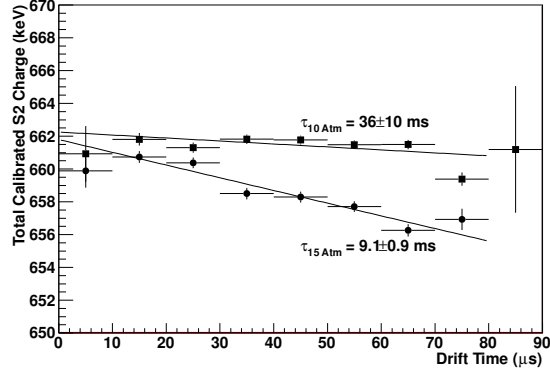


Figure 9: **Electron attachment losses:** The average calibrated S2 charge versus the charge-weighted drift time is shown for full energy events. Attachment lifetimes are obtained from the shown exponential fits. The 10 atm data was taken with a 0.19 kV/cm field in the drift region and the 15 atm data with 0.59kV/cm.

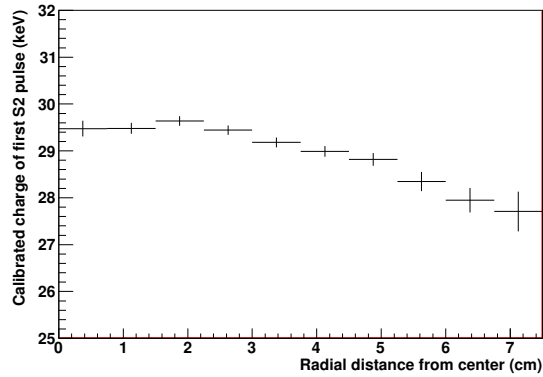


Figure 10: **Radial dependence of energy response:** Xenon x-ray energy depositions were selected from full-energy 662 keV events for which the first S2 pulse has energy in the 20-40 keV range. The reduced response at larger radial positions (also observed in a detailed Monte Carlo simulation of the TPC) is due to geometric and optical effects of the EL light collection efficiency. These data were taken at 10 atm with a 1.0 kV/cm field in the drift region and 2.68 kV/(cm atm) in the EL region.

388 due to the large coulomb multiple scattering in xenon. Figure 11 shows the
 389 effect of a radial cut on the energy resolution of 662 keV depositions and
 390 its efficiency. Since the collimated gamma rays enter the chamber along the
 391 main axis, events with a small average radial position have better energy
 392 resolution primarily because they span a smaller radial range.

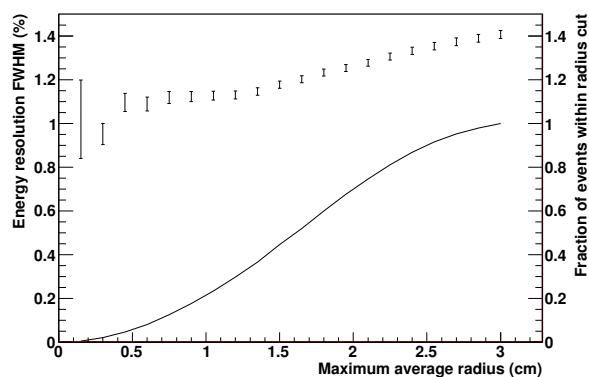


Figure 11: **Energy resolution dependence on radial cut:** Full energy 662 keV events are chosen and, for each, an average x-y position is computed (and scaled to true TPC coordinates) using all of the S2 signal. The FWHM energy resolution (data points) is obtained from a gaussian fit to the peak after placing a cut on the radial position (the abscissa). The radial cut efficiency (solid line and right ordinate axis) is also shown. These data were taken at 10 atm with a 0.16 kV/cm field in the drift region and 2.1 kV/(cm atm) in the EL region.

393 Figure 12 shows the improvement in the measured energy resolution for
 394 662 keV depositions with increased EL light yield. As seen in Eq. 2 and 3
 395 the G term dominates the resolution at low light yields (n_{pe} small) while the
 396 intrinsic Fano term is the asymptotic resolution in the large light yield limit.

397 In Fig. 13 the energy spectrum in the 662 keV full energy region obtained
 398 at 10 atm is shown. A 1.1% FWHM energy resolution was obtained for

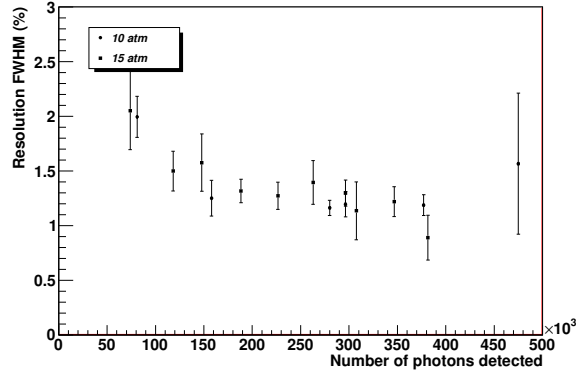


Figure 12: **Energy resolution dependence on amount of light detected:** 662 keV full energy peak resolutions are shown for data runs with different total S2 light yield (controlled primarily by the E/P in the EL region). Energy spectra were obtained by selecting events reconstructed in the central 1 cm radius region and with an S1 signal with more than 100 measured photons and not more than 600. A small electron drift-time-dependent attachment correction is applied. The expected $\sim 1/\sqrt{N}$ improvement is observed. These data were taken with drift fields of 0.5-0.6 kV/cm at 10 atm and 0.16-0.72 kV/cm at 15 atm.

399 events reconstructed in the central 0.6 cm radius region. A small drift-time
400 dependent correction for attachment losses with $\tau = 13.9$ ms was applied.
401 The xenon x-ray escape peak is clearly visible ~ 30 keV below the main
402 peak. For the spectrum taken at 15 atmospheres, shown in Fig. 14, a 1%
403 FWHM resolution was obtained. At this higher pressure the xenon x-ray
404 is less likely to escape from the active volume and the escape peak almost
405 disappears. This resolution extrapolates to 0.52% FWHM at $Q_{\beta\beta}=2.458$
406 MeV if the scaling follows a statistical $1/\sqrt{E}$ dependence.

407 In order to study the EL TPC energy resolution at lower energies, full
408 energy 662 keV events that had a well separated x-ray pulse reconstructed

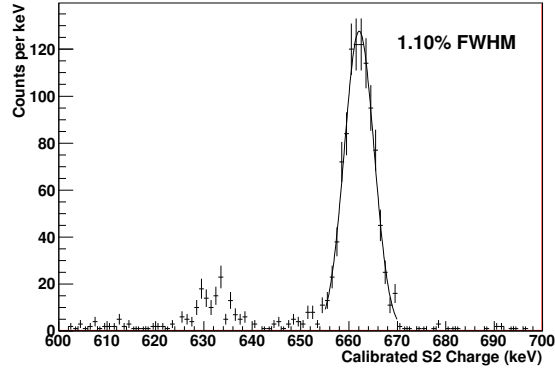


Figure 13: **Energy resolution at 10 atm for 662 keV gamma rays:** These data were taken at 10.1 atm with a 0.16 kV/cm field in the drift region and 2.08 kV/(cm atm) in the EL region. If assumed to follow a $1/\sqrt{N}$ dependence this resolution extrapolates to 0.57% at $Q_{\beta\beta}=2.458$ MeV.

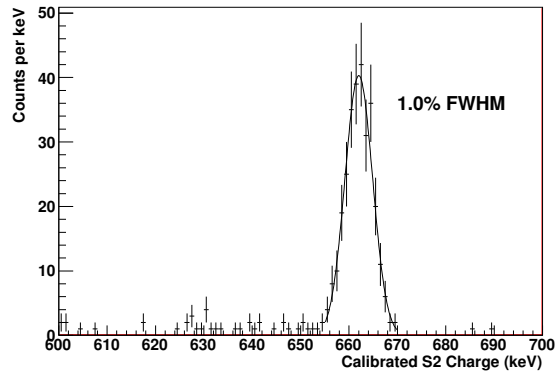


Figure 14: **Energy resolution at 15 atm for 662 keV gamma rays:** A 1.0% FWHM energy resolution was obtained for events reconstructed in the central 0.75 cm radius region. The attachment losses correction with $\tau = 9.0$ ms was applied. A PMT with a clear time varying response was removed from the measurement. These data were taken at 15.1 atm with a 0.59 kV/cm field in the drift region and 1.87 kV/(cm atm) in the EL region.

409 in the central 1.5 cm radius region were used. The energy calibration was
 410 done on the 662 keV full energy peak and linearity with a zero intersect was
 411 assumed. Figure 15 shows the energy spectrum obtained at 10 atm with a
 412 5% FWHM resolution. The spectrum was fit to the sum of four gaussians
 413 with relative positions and intensities fixed to the strongest xenon x-ray lines
 414 [?]. The absolute position of the anchor peak and the peaks' widths (all
 415 assumed the same) were obtained from the fit. The anchor peak is at 29.1
 416 keV, less than 2% away from its nominal 29.6 keV value.

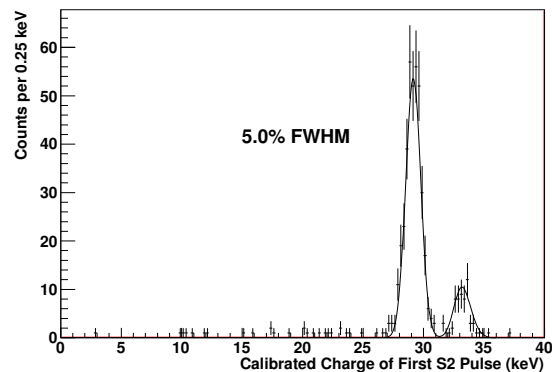


Figure 15: **Energy resolution at 10 atm for 30 keV xenon x-rays:** A 5% FWHM energy resolution for 30 keV was obtained. These data were taken at 10.1 atm with a 1.03 kV/cm field in the drift region and 2.68 kV/(cm atm) in the EL region.

417 Figure 16 summarizes our measurements and understanding of the EL
 418 TPC energy resolution. The lower diagonal line represents the Poisson statisti-
 419 cal limit from the measurement of a small fraction of the photons produced
 420 by the EL gain while the upper diagonal line includes the degradation (mostly
 421 from PMT afterpulsing) due to PMT response. The circle data points show
 422 the energy resolutions obtained for dedicated LED runs with varying light

423 intensities per LED pulse. The LED points follow the expected resolution
424 over the two decades range studied. The two horizontal lines represent the
425 xenon gas nominal intrinsic resolution for 30 and 662 keV, respectively, and
426 the two curved lines are the expected EL TPC resolutions with contributions
427 from the intrinsic limit and the photons' measurement. Our 662 keV data
428 (squares) and xenon x-ray data (triangles) taken with various EL gains follow
429 the expected functional form of the resolution but are 20-30% larger possi-
430 bly due to the x-y response non-uniformity. Detailed track imaging from a
431 dense photosensor array near the EL region, such as the one being currently
432 commissioned for the NEXT-DBDM prototype, will enable the application
433 of x-y position corrections to further improve the energy measurement.

434 In Ref. citeBolotnikov, a study of the energy resolution for 662 keV
435 gamma rays at pressures near condensation (30 atm and above) using a xenon
436 ionization chamber found an improvement of the resolution for increased drift
437 fields. Asymptotic optimum resolutions were achieved only after applying 4
438 kV/cm or larger fields. Since these large fields would be difficult to achieve
439 in a detector with one meter long drift region such as the one planned for
440 NEXT-100, we investigated the resolution dependence on the drift electric
441 field at 10 atm. Figure 17 shows no discernible dependence in the 0.16-1.03
442 kV/cm region investigated.

443 *7.4. EL TPC characterization: light yield, drift velocity and longitudinal dif-* 444 *fusion*

445 While the study of the energy resolution achievable in the EL TPC was
446 the main goal of this work, we pursued other measurements as well as cross
447 checks against previous results by others. Figure 18 shows the linearity of

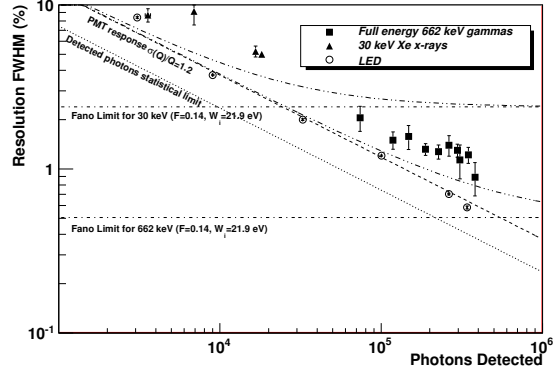


Figure 16: **Energy resolution in the high-pressure xenon NEXT-DBDM electroluminescent TPC:** Data points show the measured energy resolution for 662 keV gammas (squares), ~ 30 keV xenon x-rays (triangles) and LED light pulses (circles) as a function of the number of photons detected. The expected resolution including the intrinsic Fano factor, the statistical fluctuations in the number of detected photons and the PMT charge measurement variance is shown for x-rays (dot dot dashed) and for 662 keV gammas (dot dot dot dashed). Resolutions for the 662 keV peak were obtained from 15.1 atm data runs while x-ray resolutions we obtained from 10.1 atm runs.

448 the EL light yield as the E/P in the 0.5 cm EL region is varied from 1
 449 to 2 kV/(cm atm) at 15 atmospheres and from 1 to 3 kV/(cm atm) at 10
 450 atmospheres. At these pressures xenon deviates from the ideal gas behavior
 451 at the 10% level. Therefore, the more appropriate variables to describe the
 452 process are density (N) and reduced electric field (E/N). Figure 19 shows the
 453 density normalized EL yield as a function of the reduced field. As expected,
 454 points from the 10 and 15 atm data sets follow the same linear trend with
 455 consistent slope and threshold.

456 The electron drift velocity was obtained from the maximum drift times
 457 measured (which correspond to the full drift length of 8 cm) for x-ray energy

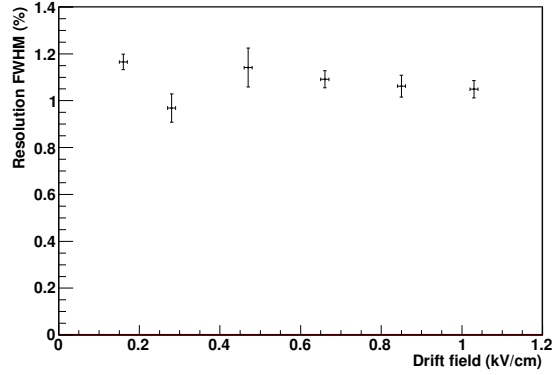


Figure 17: **Energy resolution dependence on drift field:** These data were taken at 10.1 atm with 2.1 - 2.7 kV/(cm atm) in the EL region. The energy resolution attained is largely independent of the drift electric field in the investigated range.

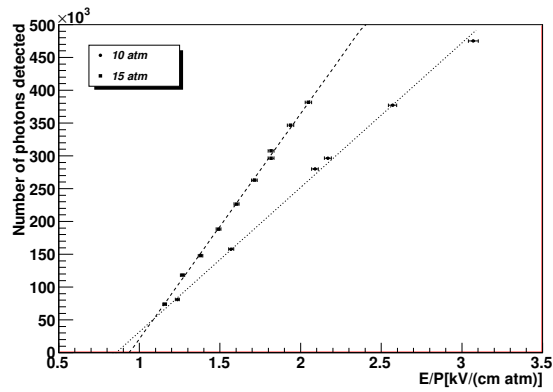


Figure 18: **Light yield dependence as a function of E/P in the EL region**

458 depositions. Figure 20 shows the drift velocity measured for various drift
 459 fields along with two Monte Carlo calculations using up-to-date xenon-
 460 electron collision cross sections. While the data points follow the trend in
 461 the calculations, 10% deviations are seen at the lower drift fields. Yet, the
 462 general agreement observed validates the pressure and field measurements as

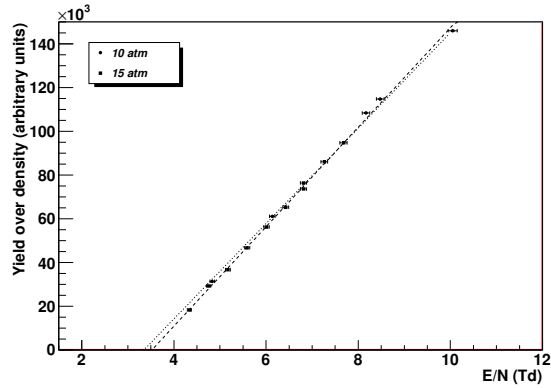


Figure 19: Density normalized light yield vs. EL reduced field.

463 well as the drift field uniformity and the xenon purity.

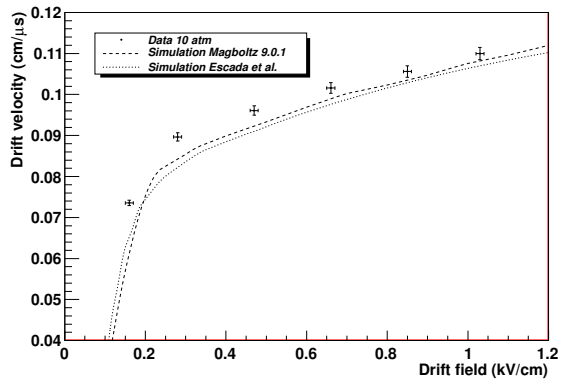


Figure 20: **Drift velocity dependence on drift field:** These data were taken at 10.1 atm.

464 The longitudinal diffusion was calculated from the time spread of EL light
 465 of x-ray depositions (see example fits in the upper right insets of Figs. 4 and
 466 5) and using the measured drift velocity. For x-ray pulses with long drift
 467 times the longitudinal diffusion is the dominant source of pulse width with
 468 subdominant contributions from the transit time of electrons through the EL

469 gap and from the ionization track length. Figure 21 shows the dependence
470 of the longitudinal diffusion on the drift field and the corresponding Monte
471 Carlo calculations that mostly bracket the data.

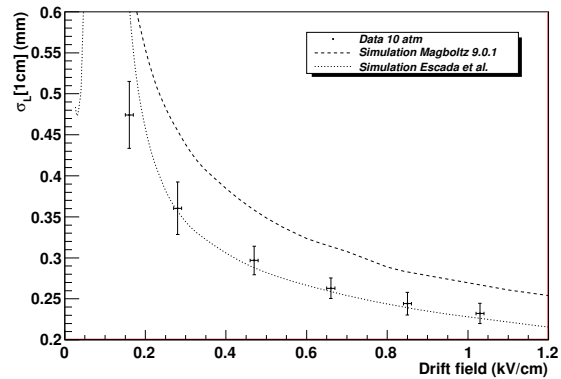


Figure 21: **Longitudinal diffusion dependence on drift field:** The measured longitudinal diffusion is presented here as the σ spread along the drift direction for a 1 cm drift. These data were taken at 10.1 atm.

472 *7.5. S1 measurement*

473 Unlike the S2 light which is generated within a small 0.5 cm region in z,
474 the S1 photons are produced throughout the entire TPC volume wherever
475 the primary ionization happened. As a result the S1 charge (number of
476 photons detected) shows large event-by-event variations. S1 light collection
477 efficiency is largest for events closer to the PMT array due to the larger solid
478 angle. Figure 22 shows the S1 signal's dependency on the average z position
479 of the event. Between 0.2 and 0.45 S1 photons are detected per keV of energy
480 deposited. This S1 yield is consistent with the known W_s , the average energy
481 loss required to liberate one primary scintillation photon in gaseous xenon[?
482], and the photon collection and detection efficiency in our TPC. S1 photons
483 are produced from direct excitations of xenon atoms by the ionizing particle
484 and by ion-electron recombinations. The latter component is, in general, field
485 and pressure dependent. Figure 22 shows less than 10% differences between
486 the S1 yield of runs taken with reduced fields of 0.04 and 0.10 kV/(cm atm)
487 in the drift region.

488 **8. Comparison with Expectations and Simulations?**

- 489 Compare with resolution formula?
- 490 Compare spectra with MC?
- 491 Compare Position distributions with MC?

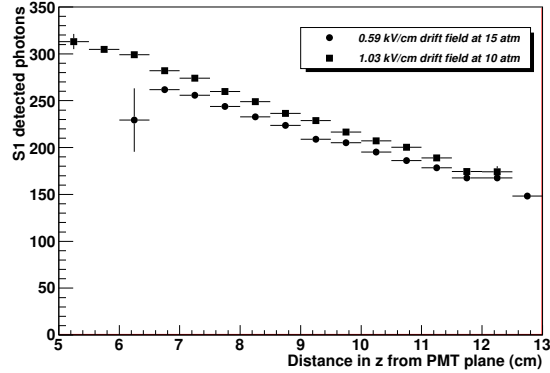


Figure 22: **S1 signal dependence on z position:** For events with full energy 662 keV depositions, the number of measured S1 photons is shown versus the average distance of the ionization track from the PMT plane (obtained from the S2 charge-weighted drift time and the measured drift velocity). The Two runs are shown with E/P in the drift region of 0.04 and 0.10 kV/(cm atm) with very similar S1 yield.

492 **9. Future Developments and Plans**

493 **10. Conclusions**

494 **11. Acknowledgements**

495 NERSC, KA15, NS?

496 [1] E. Majorana, Theory of the Symmetry of Electrons and Positrons, Nuovo
497 Cim. 14 (1937) 171–184. doi:10.1007/BF02961314.

498 [2] A. Bolotnikov, B. Ramsey, The spectroscopic properties of high-
499 pressure xenon, Nucl. Instr. and Meth. A 396 (3) (1997) 360 – 370.
500 doi:10.1016/S0168-9002(97)00784-5.